Compacted Graphite Iron: Mechanical and Physical Properties for Engine Design

Dr. Steve Dawson

SinterCast
— Supermetal CGI —

1 Introduction

As the demand for high torque, low emissions and improved fuel economy continues to grow, engine designers are forced to seek stronger materials for engine block construction. This is particularly true in the diesel sector where resolution of the conflicting performance objectives requires increased cylinder bore pressures. The bore pressures in today's direct injection diesels hover around 135 bar while the next generation of DI diesels are targeting 160 bar and beyond. Peak combustion pressures in heavy duty truck applications are already exceeding 200 bar. At these operating levels, the strength, stiffness and fatigue properties of grey cast iron and the common aluminum alloys may not be sufficient to satisfy performance, packaging and durability criteria. Several automotive OEM's [1-3] have therefore evaluated Compacted Graphite Iron (CGI) for their petrol and diesel cylinder block and head applications.

Although compacted graphite iron has been known for more than forty years, and several review papers have been published [4-11], the properties of CGI are not yet as well known as those of grey cast iron and the common aluminum alloys. This paper therefore provides more detailed information on the mechanical and physical properties of CGI as a function of the graphite nodularity, carbon content and the influence of ferrite and pearlite. The data presented are primarily from tests conducted at independent laboratories, although literature data is included and referenced where appropriate.

2 Microstructural Considerations

As shown in Figure 1, the graphite in compacted graphite iron (sometimes referred to as vermicular iron) appears as individual 'worm-shaped' or vermicular particles. Although the particles are elongated and randomly oriented as in grey iron, the compacted graphite particles are shorter and thicker, and have rounded edges. While the compacted graphite particle shape may appear worm-like when viewed with a conventional light microscope, deep-etched SEM micrographs (Figure 2) show that the 'worms' are connected to their nearest neighbours within the eutectic cell. This complex graphite morphology, together with the rounded edges and irregular bumpy surfaces, results in strong adhesion between the graphite and the iron matrix. Ultimately, the compacted graphite morphology inhibits both crack initiation and propagation and is the source of the improved mechanical properties relative to grey cast iron.
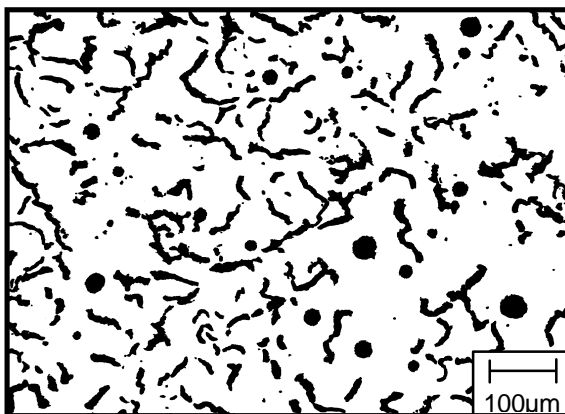

Figure 1: Compacted Graphite Iron microstructure with 10% nodularity
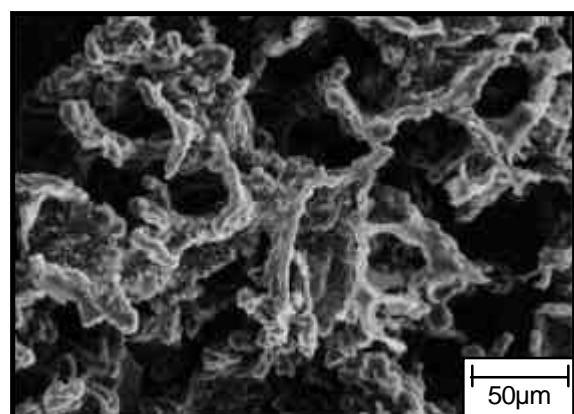

Figure 2: Deep-etched SEM micrographs show the true three dimensional graphite morphology

The percent nodularity of all test specimens was evaluated by image analysis using the criteria described in Reference [12]. The micrograph presented in Figure 1 has a calculated nodularity of 10%. In addition to the influence of nodularity, the presence of graphite flakes or discrete patches of flake-type graphite also impacts upon the mechanical and physical properties of CGI. In order to allow the data obtained from flake-containing microstructures to be plotted together with data from CGI and nodular microstructures, the present study introduces a nodularity range of 0 to -5% nodularity to represent the amount of flake graphite present in the otherwise compacted microstructure. Specimens containing isolated patches of flake graphite are assigned nodularity ratings ranging from -1 to -5% with increasingly negative values representing increasing severity of flake patch occurrence. A value of 0% nodularity corresponds to a fully compacted structure, while -5% represents a fully flake graphite microstructure. The abrupt step from 0% nodularity for CGI to -5% nodularity for grey iron is intentionally chosen to parallel the rapid transition from a fully compacted microstructure to a flake-containing structure. In practice, this transition can occur due to a decrease of only 0.001% magnesium in the molten cast iron. A flake patch micrograph with an assigned value of -3% nodularity is presented in Figure 3 as a visual reference.
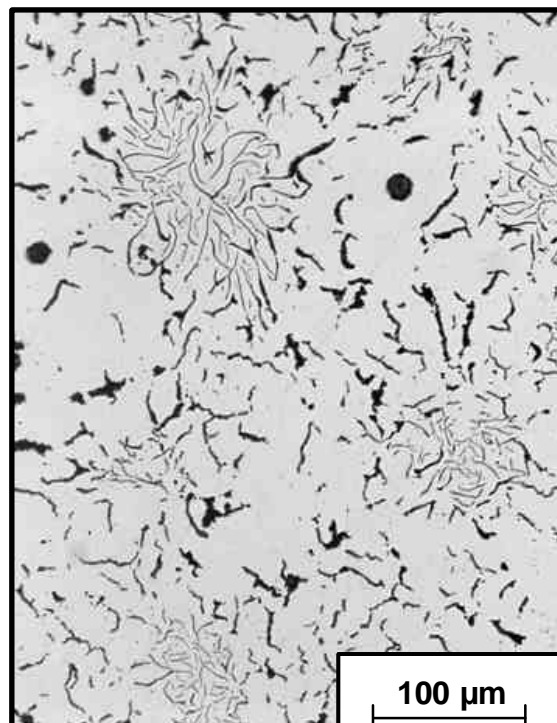

Figure 3: *Insufficient Magnesium treated leads to isolated flake patches in the compacted graphite micro-structure. This micrograph is assigned a value of -3% nodularity*

Finally, the pearlite content of the test specimens was evaluated visually with the criteria that pearlite-plus-ferrite must equal 100%. Cementite (carbide) was not present in any of the test pieces. All microstructure results are obtained directly from the test pieces after the relevant mechanical or physical property has been evaluated. The nodularity and pearlite results represent the average value of at least three fields of view (>10 mm² total area) subjectively chosen to represent the bulk microstructure of the test piece.

3 Test Piece Production

The data presented in this paper were obtained from standardised test pieces produced in a production foundry. The base iron was melted in 6 tonne coreless medium frequency induction furnaces and held in a 60 tonne coreless line frequency furnace as part of the standard base iron for ductile iron series production. Base treatment was performed with a commercially available MgFeSi alloy followed by SinterCast analysis and corrective additions of 5 mm magnesium and/or 9 mm diameter inoculant cored wires to obtain the desired graphite shape. Test pieces were poured from a one-tonne production ladle. Specific details of test piece geometry, chemistry and microstructure are provided in each section of the paper as appropriate.

4 Tensile Properties

The test pieces used for tensile testing were machined from as-cast cylindrical test bar samples produced according to the ASTM A 536 standard. Three tensile specimens were machined from each bar. The tensile tests were conducted by the ABB Corporate Research laboratories in Västerås Sweden using a Wolpert 100 kN:s universal testing machine according to the ASTM E 8M (room temperature) and ASTM E 21 (elevated temperature) norms. The individual results presented in this section represent the average of two separate 'pulls' for the room temperature data and three separate 'pulls' for the data at 100°C and 300°C. A total of 84 tensile tests were performed.

The experimental design of the tensile tests was established to focus on the most relevant microstructures for the production of CGI cylinder blocks and to identify the variation in tensile properties as the microstructure strays beyond the desired range. Thus, the materials studied can be separated into two categories:

1   CGI with fixed (0-10%) nodularity and as-cast matrix structures ranging from 20-100% pearlite, and

2   CGI with fixed (85-100%) as-cast pearlite content and graphite shape ranging from mixed CGI/flake-patch structures up to 90% nodularity.

Eleven different microstructure Groups were evaluated to represent the total range of cast iron microstructures. The microstructure data and chemical composition for the eleven different microstructure Groups are summarized in Table I while the tensile results are presented in Table II.

The change in the ultimate tensile and the 0.2% yield strength of predominantly (85-100%) pearlitic cast irons as a function of nodularity is shown in Figure 4. While the strength gradually increases with increasing nodularity, the presence of even a small amount of flake graphite results in a step-reduction of 20-25% tensile strength. Extrapolation of the data suggests that a fully A-Type flake structure would have a room-temperature tensile strength of approximately 200 MPa at the carbon content required to produce CGI. It is apparent from these results that flake graphite must be avoided in CGI castings.

Table I
Chemistry and microstructure data for tensile specimens

Group Number	Nodularity (%)	Pearlite (%)	Chemical Analysis(%)									
			C	Si	Mn	S	Mg	Cu	Sn	Cr	Al	P
1	4	25	3.63	2.49	0.42	0.014	0.007	0.42	0.039	0.02	0.008	0.010
2	4	45	3.54	2.49	0.41	0.010	0.007	0.40	0.040	0.02	0.003	0.011
3	8	50	3.54	2.50	0.41	0.012	0.010	0.41	0.040	0.02	0.003	0.011
4	7	75	3.61	2.49	0.40	0.014	0.008	0.45	0.053	0.03	0.004	0.011
5	6	94	3.59	2.48	0.39	0.013	0.011	0.71	0.094	0.03	0.007	0.011
6	-3	86	3.60	2.45	0.40	0.014	0.008	0.45	0.051	0.03	0.004	0.010
7	-2	93	3.57	2.48	0.39	0.014	0.006	0.72	0.094	0.03	0.008	0.010
8	0	99	3.58	2.48	0.39	0.016	0.010	0.71	0.094	0.03	0.008	0.010
9	33	87	3.57	2.50	0.40	0.011	0.023	0.41	0.039	0.03	0.003	0.011
10	67	90	3.50	2.47	0.41	0.010	0.027	0.44	0.052	0.02	0.003	0.011
11	80	90	3.58	2.50	0.39	0.012	0.030	0.72	0.095	0.03	0.007	0.011

Table II
Summary of tensile results as a function of temperature

| Group Number	Nodularity (%)	Pearlite (%)	BHN (10/3000) (25°C)	UTS (MPa)			0.2% YS (MPa)			E. (GPa)			Elong (%)		
				25	100	300	25	100	300	25	100	300	25	100	300
1	4	25	158	298	289	270	232	220	210	138	128	139	4.0	3.1	1.6
2	4	45	174	340	314	303	261	238	240	137	126	130	3.5	2.7	1.1
3	8	50	200	332	324	299	253	239	243	143	--	--	--	1.5	1.5
4	7	75	219	435	419	377	316	295	284	147	160	132	3.5	2.4	1.4
5	6	94	234	475	472	429	347	333	324	147	144	132	1.5	1.5	1.0
6	-3	86	202	300	285	242	232	219	195	120	124	84	2.8	1.3	0.9
7	-2	93	219	347	316	--	273	256	220	134	114	90	1.5	0.7	0.7
8	0	99	239	440	422	391	324	308	299	148	147	142	1.5	1.1	0.9
9	33	87	239	567	533	497	359	317	300	162	172	136	4.3	3.0	3.3
10	67	90	244	649	602	566	370	337	325	168	166	159	5.8	6.9	5.0
11	80	90	239	715	672	626	412	359	347	168	151	158	5.8	6.6	4.2
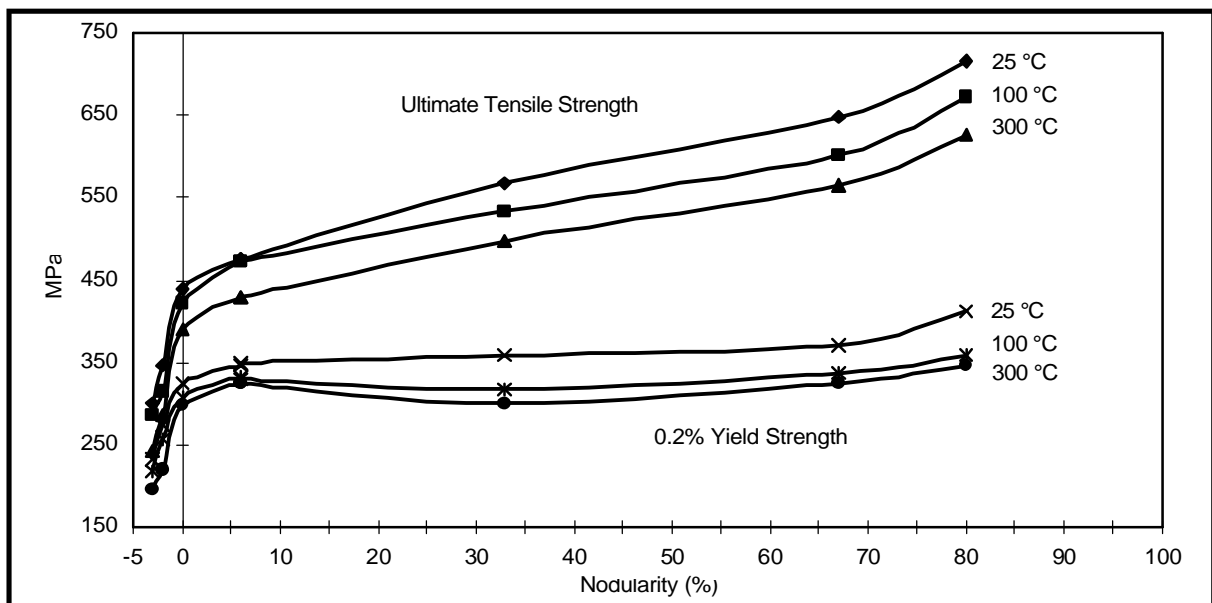
Figure 4: Ultimate tensile strength and 0.2% yield strength of 85-100% pearlitic cast irons as a function of nodularity and temperature

SinterCast
— Supermetal CGI —

The data of Figure 4 also indicate the effect of increasing nodularity which occurs naturally due to increased cooling rates in the thin sections of a casting. The gradual increase in tensile strength with increasing nodularity is validated by extrapolation of the 25°C line which tends toward 750 MPa for pearlitic ductile (>90% nodularity) iron. However the 0.2% yield strength was measured to only increase by 5% over the range of 0 to 50% nodularity. Other literature sources report 10% [4] and 20% [8] increases in yield strength over the same nodularity range. Regardless of the actual amount, the strength increase from 0 to 50% nodularity is gradual rather than a step function.

The tendency toward increased graphite nodularity and thus increased strength in thin sections may at first appear contrary to the traditional approach to grey iron engine design, which requires graphite homogeneity throughout the casting. With grey iron, thin sections become naturally weaker. However, the increase in the strength of thin-section CGI may be beneficial in many product applications. In the specific example of passenger car cylinder blocks, 'thin' means less than approximately 4.5 mm. If the remaining 'thick' sections of the block contain 5-15% nodularity, the thin sections may contain 30-60% nodularity depending on the gating system, their location and thus their cooling rate. As the thin walls are typically water jacket housings, crankcase housings and ribs, there are no thermal or machining requirements and the increased strength and stiffness of the higher nodularity material benefits the product. Microstructually inhomogeneous products are not uncommon in the industry and include some cylinder liners, flywheels, glass bottle molds and even the extreme examples of cast iron liners in aluminum cylinder blocks and ductile iron bearing caps or bedplates in grey iron cylinder blocks. Specific materials are used where their properties can best contribute to the performance of the finished component. The natural tendency of CGI toward higher nodularity in thin sections provides opportunities to place thermally efficient low-nodularity CGI in the central portions of a cylinder block and higher strength higher nodularity microstructures in the mechanically loaded areas. Indeed, this approach has been advocated in recent inhomogeneous graphite cylinder block patents and patent applications from Mazda [13] and Ford [14].

The influence of pearlite content on the tensile and 0.2% yield strengths of 0-10% nodularity CGI (Figure 5) is linear with R-squared correlation coefficients in excess of 0.95. In consideration of the normal variation in mechanical property test results, and particularly in the visual determination of pearlite content, it appears that a 20% pearlite specification range (for example, 60 to 80% pearlite with a target of 70% pearlite) will result in a 10-15% range of ultimate tensile strength. In the final analysis the pearlite specification for most applications should be based on hardness, wear and machinability considerations rather than tensile properties.

With regard to elongation, the data presented in Table II clearly show the ductile nature of CGI and the fact that elongation increases with increasing nodularity and decreasing pearlite content. The data presented in Table II are in good agreement with data published in the open literature [15].
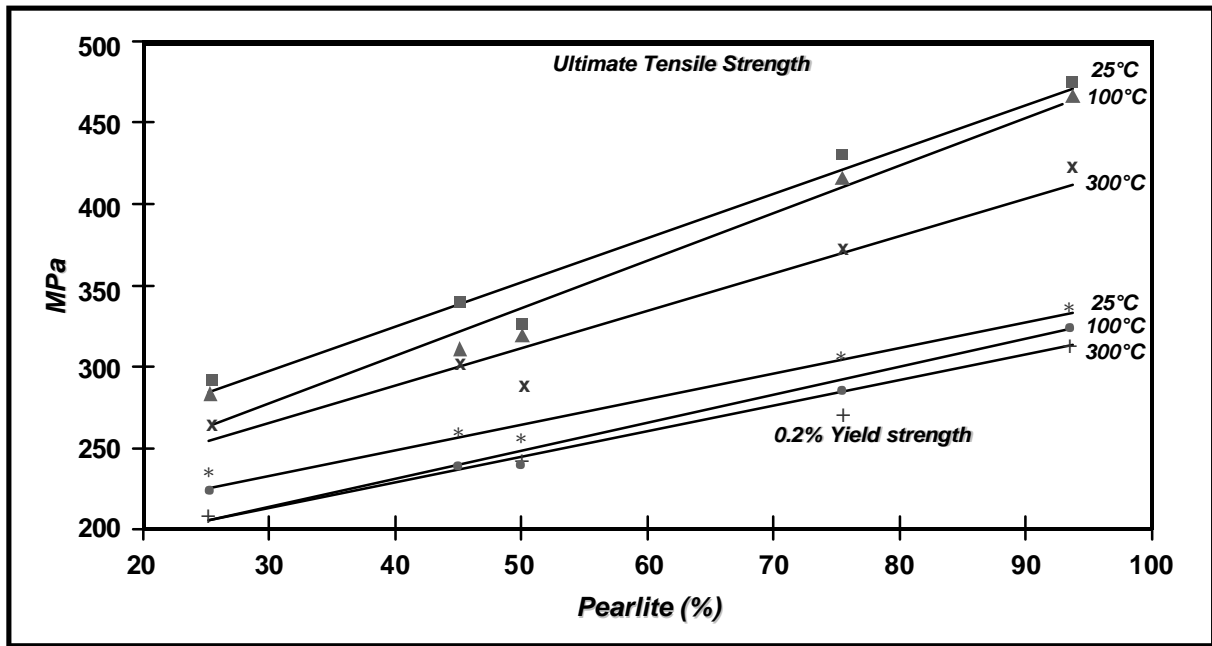
Figure 5: Ultimate tensile strength and 0.2% yield strength of 0-10% nodularity CGI as a function of pearlite content

As shown in Figure 6, the variation in elastic modulus as a function of graphite nodularity is similar to that observed for tensile and yield strength. The presence of even a small amount of flake patches reduces the elastic modulus of CGI by as much as 20%. While the elastic modulus of conventional pearlitic grey iron ranges from 105-110 GPa, interpolation of the room temperature data in Figure 6 suggests the elastic modulus of a fully A-Type flake structure produced with CGI base iron chemistry would be less than 100 GPa. Again, flake graphite must be avoided.
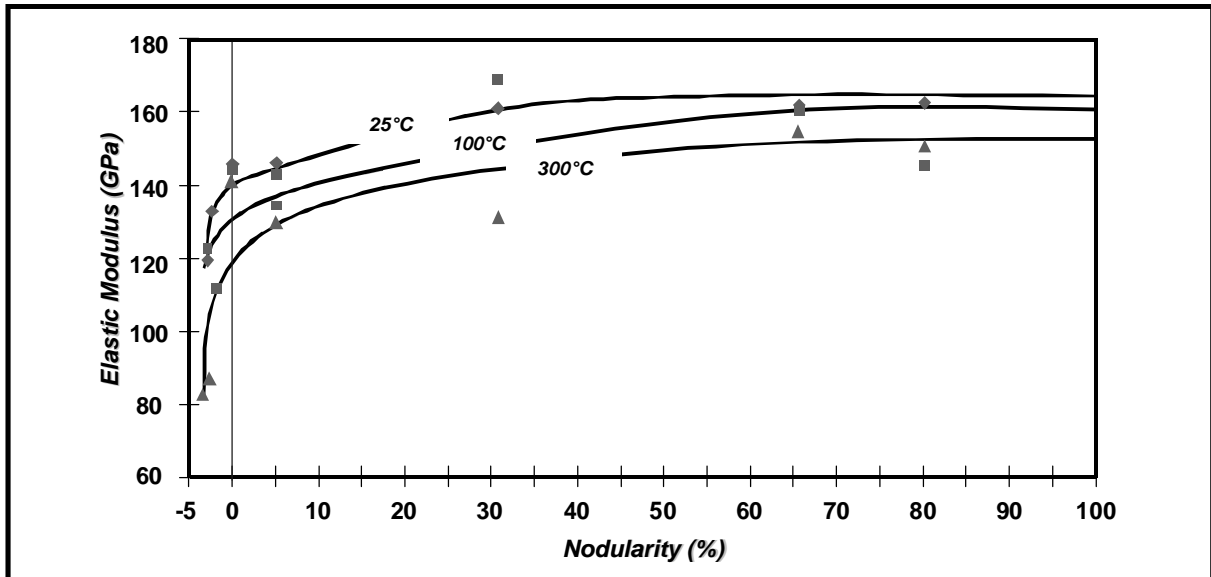

Figure 6: Elastic Modulus of 85-100% pearlite cast irons as a function of nodularity and temperature

The data presented in Table II show that the elastic modulus of 0-10% nodularity CGI is constant in the range of 145-150 GPa for pearlite contents above approximately 50%. The modulus gradually decreases at lower pearlite contents and increases with increasing nodularity.

Another important design consideration regarding the elastic modulus of CGI is that, unlike grey iron, the elastic modulus of CGI remains constant in the presence of applied tensile stress and elevated temperatures [16]. As shown in Figure 7, because grey iron does not elongate when subjected to tensile stress, it immediately experiences a linear decrease in elastic modulus when subjected to tensile stress. In contrast, ductile materials such as CGI and steel iron have a distinct range of proportionality between stress and strain and thus maintain a constant elastic modulus until a certain temperature-dependent stress limit is reached. The modulus then decreases in a linear manner. The practical significance of this is that the actual elastic modulus (stiffness) of dynamically loaded CGI components can be 50-75% higher than identically designed and loaded grey iron components.
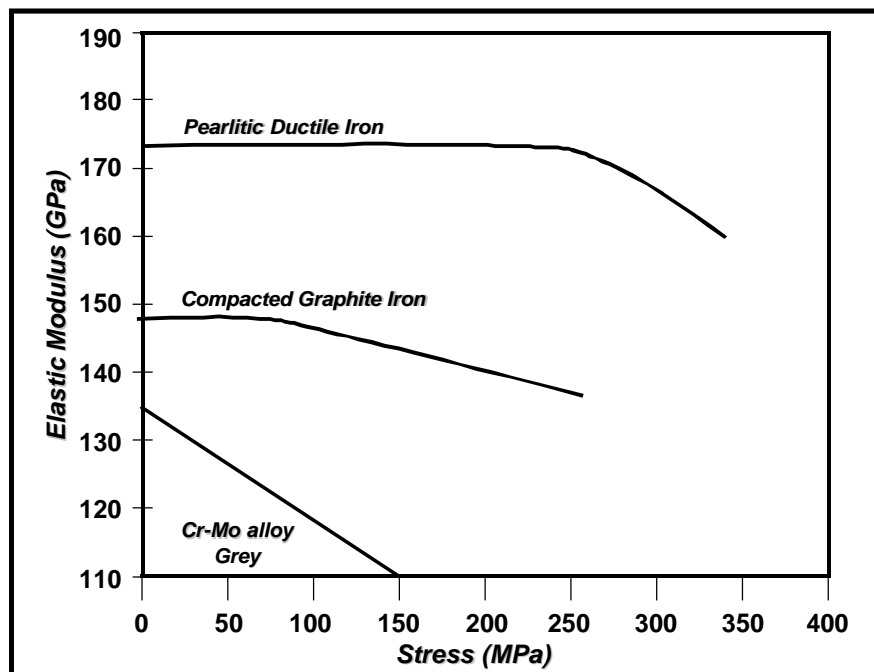

Figure 7: The elastic modulus of pearlitic Cr-Mo alloyed grey iron, pearlitic CGI and ductile iron as a function of applied tensile load and temperature. After [7]

5 Compression Properties

The compressive yield strength of cast irons plays an important role in determining the thermal fatigue life of constrained components, particularly for the valve-bridge area of heavy-duty diesel engine cylinder heads. The 0.2% compressive yield strength of unalloyed and Cr-Mo alloyed compacted graphite irons was therefore evaluated together with a pearlitic grey cast iron according to the DIN 1691 standard for GG25.

The compression tests were conducted at the Swedish National Testing and Research Institute (Sveriges Provnings-och Forskningsinstitut) in Gothenburg, Sweden. The tests were conducted at room temperature and 400°C according to the ASTM E 9 standard with 'medium' length test bars. All test specimens were produced in the manner previously described for the tensile specimens. The microstructure and chemistry details of each test material are presented in Table III while the compressive properties are summarised in Table IV. The results reported for compressive yield strength and elastic modulus represent the average of three individual compression tests.

Table III

Chemical and microstructural details of compression test specimens

Sample Number	Sample Description	Nodularity (%)	Pearlite (%)	Chemical Analysis(%)								
				C	Si	Mn	S	Mg	Cu	Sn	Cr	Mo
1	Pearlitic Grey	A-Flake	100	3.25	1.91	0.70	0.08	0.001	0.20	0.003	0.12	0.01
2	70% P CGI	10	70	3.73	2.35	0.39	0.013	0.009	0.55	0.04	0.03	<0.001
3	100% P CGI	5	98	3.66	2.26	0.42	0.012	0.009	0.67	0.07	0.02	<0.001
4	60% P Mo-CGI	5	60	3.63	2.33	0.37	0.013	0.010	0.55	0.03	0.03	0.27
5	100% P Mo-CGI	5	100	3.74	2.35	0.38	0.013	0.012	0.56	0.18	0.03	0.26
6	Cr-Mo CGI	5	90	3.70	2.23	0.41	0.015	0.011	0.42	0.04	0.24	0.28

Table IV

Compressive properties of the irons presented in Table III

Sample Number	Sample Description	Hardness (BHN 5/750)	E-Modulus (GPa @ 20°C)	0.2% Y.S. (MPa @ 20°C)	0.2% Y.S. (MPa @ 400°C)
1	100% Pearlitic Grey	190	119	349	297
2	70% Pearlite CGI	207	136	409	332
3	100% Pearlite CGI	240	156	437	370
4	60% Pearlite Mo-CGI	190	146	385	312
5	100% Pearlite Mo-CGI	255	148	478	394
6	90% Pearlite Cr-Mo CGI	235	150	432	360

The compression results show that the compressive yield strength of unalloyed pearlitic CGI is approximately 25% higher than that of the Cr-Mo alloyed grey iron. The data also show that the room temperature compressive yield strength increases linearly with increasing pearlite content and is apparently insensitive to the effects of chrome and molybdenum alloying. The role of chrome is to stabilize pearlite at elevated (>400°C) temperatures while molybdenum improves creep and thermal fatigue performance. Finally, the compression tests show that the elastic modulus of CGI (145-155 GPa) is the same in both tension and compression.

6 Hardness

The graphite growth and carbon diffusion behaviour during solidification of compacted graphite iron naturally favours the formation of ferritic rather than pearlitic matrices. Therefore, pearlite stabilizers such as copper and tin must be added to the base iron to ensure a predominantly pearlitic matrix. The solidification behaviour of compacted graphite iron results in 10 to 15% higher hardness than grey cast iron when compared at equal pearlite contents. While a typical Brinell hardness range for fully pearlitic grey iron cylinder blocks may be BHN 179-223, fully pearlitic CGI cylinder blocks may range from BHN 192-255. Compacted graphite iron cylinder blocks containing approximately 70% pearlite have a similar hardness to fully pearlitic grey iron blocks. As shown in Figure 8, the hardness level of CGI increases linearly with increasing pearlite content. While this trend is certainly true, the slope and intercept of the linear correlation depend on the concentration of manganese, chromium, titanium and other trace elements in the raw materials as well as the casting shake-out time.
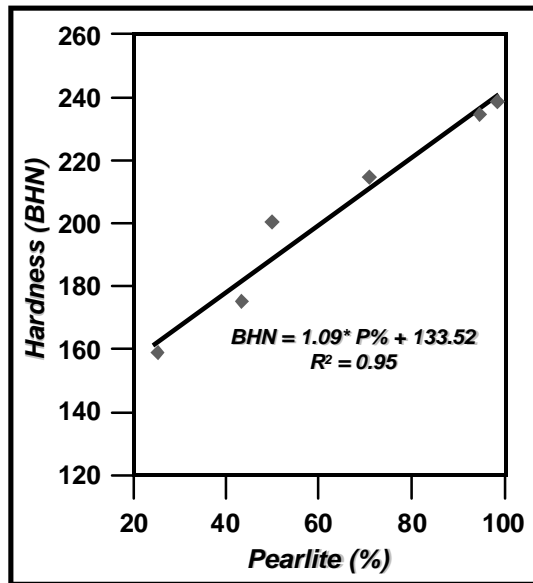
*Figure 8: Brinell hardness of unalloyed 0-10% nodularity
CGI as a function of pearlite content*

The influence of the graphite growth behaviour on hardness is evident from Figure 9. At a fixed (85-100%) pearlite content, the Brinell hardness is effectively constant from 0 to 90% nodularity. However, a step-reduction in hardness occurs as soon as flake patches begin to form. The rapid decrease in hardness between CGI and grey iron is due to the complex compacted graphite morphology which prevents slip and fracture in the matrix and at the graphite/matrix interface.
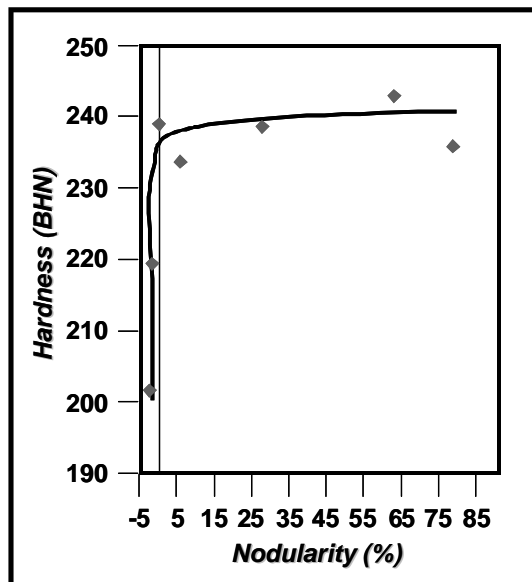

*Figure 9: Brinell hardness of 85-100% pearlitic
cast irons as a function of nodularity*

7 Wear Resistance

Wear is a complex phenomenon that comprises several tribological mechanisms and has no universally accepted test procedure or quantitative criteria for establishing the suitability of a given material. In contrast to the clearly defined specification limits for tensile properties or hardness, the wear behavior of materials is typically evaluated relative to the performance of other candidate materials. Experimental procedures can vary from sophisticated real-load simulations to relatively simple pin-on-disk or abrasion tests.

In general, unalloyed pearlitic CGI incurs approximately one-half of the wear of unalloyed pearlitic grey cast irons when exposed to scarring or abrasion conditions. Hrusovsky [17] showed that the average scar width in LFW-1 pin-on-disc tests was 45% less for pearlitic CGI than for pearlitic grey iron. Similar results have been reported for abrasion tests where the weight loss of CGI specimens during abrasion tests is 40-55% less than that of grey iron [18,19]. Although the test techniques and results vary, the consistency shows that CGI has superior wear resistance to grey iron and is a viable material for cylinder liner applications.

In order to determine the suitability of CGI as a cylinder liner material, a series of scuffing tests were conducted to compare the wear resistance of various CGI microstructures and compositions with commercially available cylinder liner materials. The scuffing test [20] was conducted by pushing a test specimen against a rotating nitrided steel cylinder. The load range and the sliding velocity (5.7 cm/sec) were selected to simulate the conditions near dead-centre in the cylinder bore of a combustion engine. Lubricant was not used in order to exacerbate the wear conditions. As the scuffing test proceeds, the surface of the test material roughens and the friction between the test piece and the nitrided cylinder increases. The relative scuffing resistance of each material is determined by comparing the lowest friction coefficient recorded, and the normal load above which the friction coefficient first exceeds 0.3. These points are known to relate to friction and scuffing behavior in internal combustion engines [20].

The chemical analysis of the four CGI variants and the conventional liner materials studied in these tests is summarized in Table V. The phosphorous-alloyed grey iron specimens and the surface-treated aluminum and grey iron specimens were sectioned from commercially available centrifugally cast cylinder liners or from the top-dead-centre sliding surface of parent bore cylinder blocks. Calibrations were made to account for the different area of surface contact for curved and flat specimens.

Table V
Chemical analysis of specimens used in scuffing tests

Sample Number	Description	Pearlite (%)	Nodularity (%)	Chemical Analysis(%)									
				C	Si	Mn	S	Mg	Cu	Sn	Cr	Mo	P
1	Ferritic CGI	20	10	3.58	2.60	0.39	0.011	0.011	0.29	--	0.03	--	0.01
2	Hypereutectic CGI	95	15	3.85	2.26	0.40	0.010	0.008	0.30	--	0.03	--	0.01
3	Cr-Mo alloyed CGI	90	15	3.76	2.23	0.40	0.013	0.013	0.41	0.04	0.28	0.28	0.01
4	Pearlitic CGI	95	10	3.60	2.29	0.40	0.013	0.012	0.74	0.07	0.03	--	0.01
5	P-alloyed Grey-I	100	--	3.05	1.76	0.67	0.061	0.006	0.16	0.01	0.34	0.19	0.48
6	P-alloyed Grey-II	100	--	3.21	2.46	0.60	0.075	0.006	0.20	0.05	0.62	0.23	0.62
7	P-B (0.1%) alloyed grey	100	--	2.90	2.40	0.70	0.10	--	0.40	--	0.30	--	0.30
8	Laser hardened grey	100	--	3.3	2.3	0.7	0.11	--	0.6	0.06	0.3	--	<0.15
9	Nicasil-coated Al	--	--	--	--	--	--	--	--	--	--	--	--

SinterCast
— Supermetal CGI —

The scuffing results plotted in Figure 10 show the minimum coefficient of friction for each material and the applied normal load at which the coefficient of friction first exceeds 0.3. Ideal wear materials should have a low coefficient of friction and simultaneously tolerate high loads without incurring wear and thus increasing friction. According to these criteria, and for the conditions of this test, the performance of unalloyed pearlitic CGI is superior to that of the Nicasil coated aluminum liner and the laser hardened and Cr-alloyed grey iron liner. The behavior of unalloyed pearlitic CGI is not statistically significantly different from the phosphorous and phosphorous-boron alloyed grey iron specimens. The best performance was realized by the Cr-Mo alloyed pearlitic CGI which simultaneously displayed the lowest friction and the highest scuffing load.
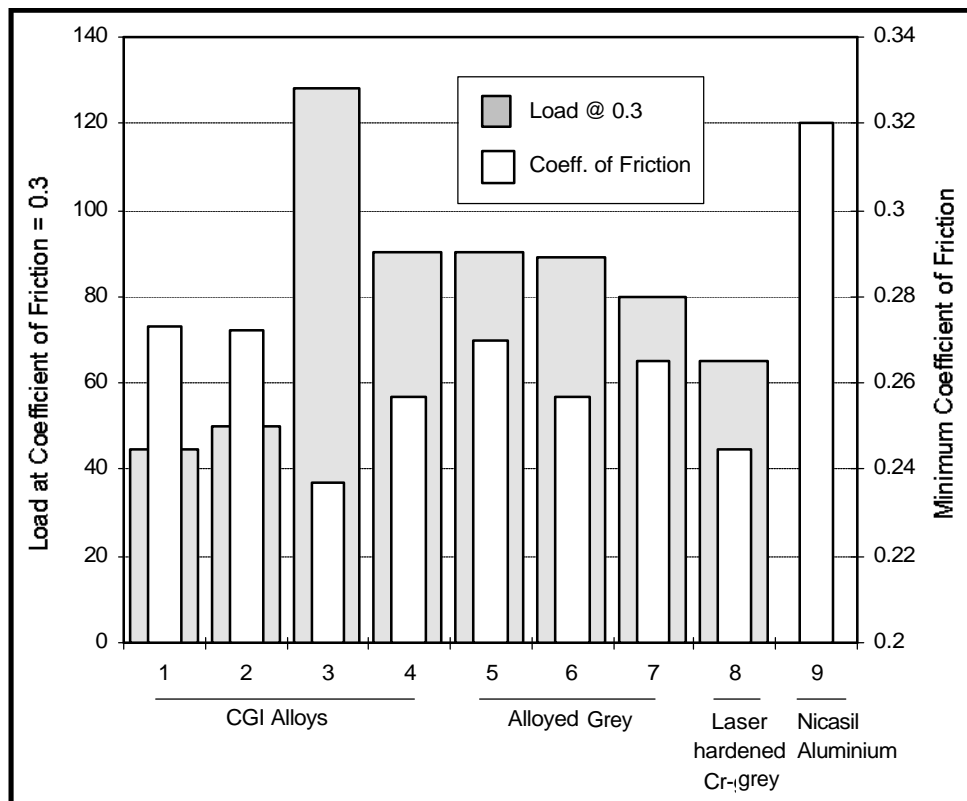

Figure 10:   *Coefficient of friction and normal load for various wear materials in scuffing bench tests*

Comparative wear tests have also been conducted by Volvo Technological Development [21] to discern the difference between unalloyed pearlitic CGI and conventional P-alloyed grey iron cylinder liners for diesel application. The engine simulation test rig pushes a standard top compression ring against a honed liner specimen with a normal load of 320 N. The ring is then oscillated with an 8 mm amplitude reciprocating motion at a frequency of 10 Hz. The contact region is submerged in used 10W/30 engine oil and heated to 80°C to replicate the wear behavior in running engines.

Operationally, the test is interrupted after three hours and the wear volume is measured by 3D profilometry to determine the running-in wear. The specimen is then repositioned and tested for a further thirteen hours to determine the steady-state wear behavior. The results of the comparative test show that the running-in (0-3 hours) and steady-state (3-16 hours) wear behavior of unalloyed pearlitic CGI is not statistically significantly different from that of the standard phosphorous-alloyed grey iron reference liners.

8 Fatigue and Notch Sensitivity

Similar to tensile properties, the fatigue strength of a material is influenced by its microstructure and alloying elements. Therefore, fatigue data should always be presented together with microstructure data and the monotonic tensile strength of the base material to serve as a reference point. Fatigue data in this section are thus reported in terms of two dimensionless indices :

$$\text{Endurance Ratio} = \frac{\text{Unnotched fatigue limit}}{\text{Ultimate tensile strength}}$$

$$\text{Fatigue Strength Reduction Factor} = \frac{\text{Unnotched fatigue limit}}{\text{Notched fatigue limit}}$$

These indices allow the notched and unnotched fatigue limits of a material to be approximated directly from its tensile strength. A summary of rotating-bending fatigue data from four different literature sources is provided in Table VI while classical S-N plots for notched and unnotched CGI are shown in Figure 11.

Table VI
Fatigue and notch sensitivity data for cast irons subjected to rotating-bending fatigue tests

Ref Number	Iron Type	Pearlite (%)	Nodularity (%)	Hardness (BHN)	UTS (MPa)	Fatigue Limit (MPa)		Endurance Ratio	Fatigue Strength Reduction Factor
						Unnotched	Notched		
22	CGI	70-80	0-10	184	388	178	100	0.46	1.77
	CGI	>90	0-10	205	414	185	108	0.45	1.72
	CGI	>90	20-300	217	473	208	116	0.44	1.80
23	CGI	<20	10-20	134	351	196	131	0.57	1.50
	CGI	>85	10-30	229	583	255	180	0.44	1.42
	SG	<20	90	159	449	226	142	0.50	1.59
	SG	>85	90	277	727	275	183	0.38	1.50
24	CGI	ferrite	--	134	248	186	137	0.58	1.36
	CGI	pearlite	--	223	346	186	118	0.45	1.57
	SG	ferrite	--	143	269	235	147	0.57	1.60
	SG	pearlite	--	223	404	255	147	0.35	1.73
25	CGI	ferrite	--	143	388	221	137	0.57	1.61
	CGI	ferrite	--	143	355	201	127	0.57	1.58
	SG	ferrite	--	137	320	196	108	0.61	1.82
	SG	ferrite	--	128	285	157	93	0.55	1.68
	Grey	ferrite	--	103	201	98	88	0.49	1.11

The literature data show that the rotating-bending Endurance Ratio of CGI ranges from 0.44 to 0.58, although values as low as 0.37 have been reported [6]. Pearlitic irons tend toward the lower end of the Endurance Limit range which means that ferritic CGI retains a larger portion of its monotonic strength in fatigue applications. Nonetheless, the absolute fatigue limit of pearlitic CGI is approximately 25% higher than that of ferritic CGI (Figure 11). The rotating-bending fatigue limit of pearlitic CGI is approximately double that of pearlitic grey iron and similar to that of ferritic ductile iron.
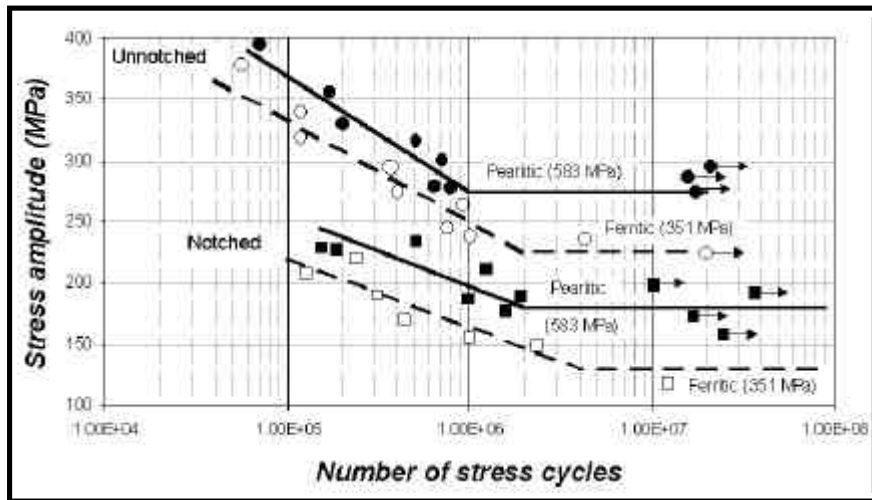
SinterCast
— Supermetal CGI —

Figure 11: S-N fatigue plot for ferritic and pearlitic CGI in rotating-bending [23]

It is well known that the notch sensitivity of cast irons is a direct function of the geometry of the imposed notch. Reference [22] employed a relatively severe 45° V-notch with a 0.25 mm root radius and obtained Fatigue Strength Reduction Factors of 1.72-1.80 for CGI. In contrast, Reference [24] incorporated a relatively smooth 'notch' geometry (actually a 1.2 mm diameter hole drilled through the centre of the test specimen) and obtained Fatigue Strength Reduction Factors ranging from 1.36 to 1.58. Finally, Reference [23] used the intermediate notch geometry of a 0.5 mm diameter by 0.5 mm deep drill hole and obtained intermediate results (1.42-1.50). While it is clear that CGI has a higher notch sensitivity than grey iron (1.05-1.15) and a lower sensitivity than ductile iron (1.50-1.85), the most critical factor is the notch geometry. Indeed, Palmer [22] states that if the root radius of the notch was increased to 5 mm in a 10.6 mm diameter fatigue specimen, the notch effect would be eliminated.

In addition to the basic data provided by conventional rotating-bending tests, designers are also interested in the fatigue behavior of components subjected to uniaxial (tension-compression) loading. This is particularly true for components which are subjected to both an underlying tensile load and cyclical stress fluctuations which are imposed about the mean tensile stress level. Depending on the mean stress level and the magnitude of the fluctuations, the resulting fatigue cycle can be either tension-tension or tension-compression. Tests of this nature are conducted with uniaxial hydraulic servo fatigue machines [26,27]. The results of such fatigue tests are presented in so-called Goodman diagrams as shown in Figure 12 [7,26] for uniaxial loading and in Figure 13 [7] for three-point bending. The fatigue limits in the absence of any mean stress can be read directly from the intersection of the fatigue limit lines with the vertical axis, while the maximum permissible stress (at 107 cycles) at any mean stress level is represented by the distance between the 45° line and the respective fatigue line for the material. Again, the performance of pearlitic CGI is similar to that of ferritic ductile iron.
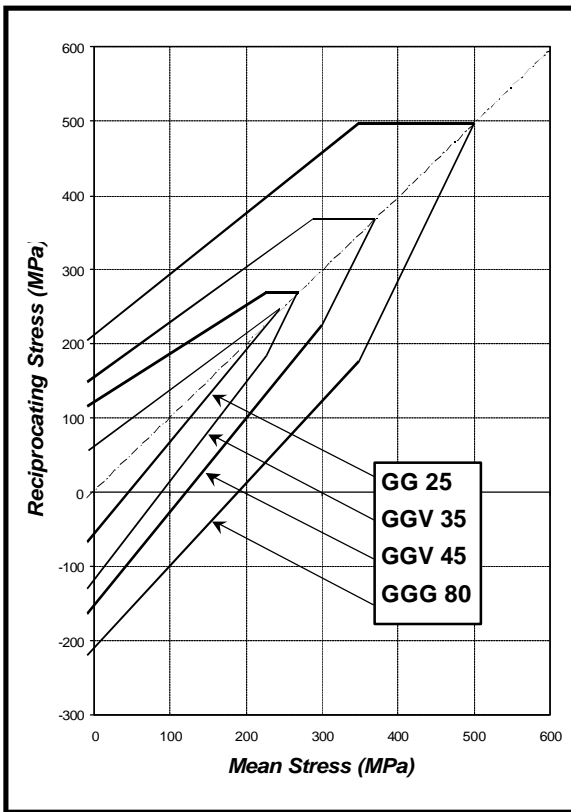
Figure 12: Goodman diagram for determination of permissible stresses under uniaxial tension-compression loading. After [7]
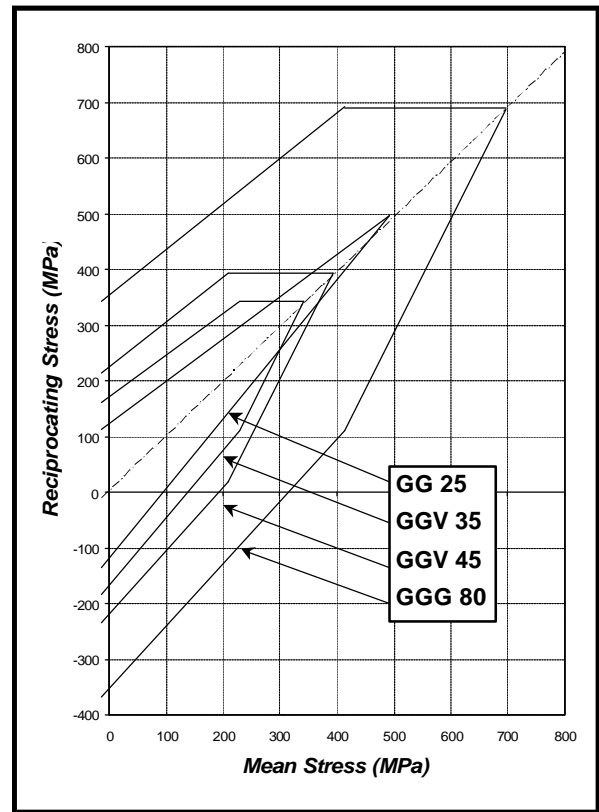

Figure 13:   *Goodman diagram for determination of permissible stresses under three point bending loads. After [7]*

The behavior of CGI under fully reversed torsional fatigue conditions has been studied by Sumimoto et al [28]. Although they only studied ferritic cast irons, their data (Table VII) show that the torsional fatigue limit of CGI is approximately the same as that of ductile iron, and thus approximately 40% higher than that of steels with similar tensile strengths. The values obtained for the Endurance Ratio of CGI are also in good agreement with that presented in Table VI for rotating-bending conditions.

<u>Table VII</u>
Fully reversed torsional fatigue data [28]

Iron Type	Matrix Condition	Hardness (BHN)	Elongation (%)	UTS (MPa)	Fatigue Limit (MPa)	Endurance Ratio
CGI	Ferrite	156	5.5	336	152	0.45
CGI	Ferrite	163	4.7	335	157	0.47
CGI	Ferrite / Pearlite	210	1.9	366	157	0.43
CGI	Ferrite	161	6.0	355	147	0.41
CGI	Ferrite	154	4.7	332	142	0.43
SG	Ferrite	156	26.3	452	186	0.41
SG	Ferrite	163	24.5	445	172	0.39
SG	Ferrite	177	23.0	498	216	0.43
Steel	Ferrite / Pearlite	114	39.2	444	130	0.29

The good fatigue performance of CGI stems directly from the compacted graphite morphology. The rounded edges of the graphite particles do not contribute to crack initiation and actually serve as crack arresters once cracks are formed. The complex coral-like morphology and irregular surfaces of the graphite particles thereafter result in good adhesion and thus present a more tortuous crack propagation path relative to the smooth flake surfaces in grey iron. These same morphological characteristics result in a two-to-four-fold increase in the thermal fatigue resistance of CGI relative to grey iron [29-31]. Despite that consistently superior thermal fatigue results have been reported for CGI under a variety of thermal cycle conditions, it must be stressed that such results may not be directly transferable to the performance of thermally loaded components such as cylinder heads. The difference in geometry, constrainment and the critical roles of thermal conductivity and elastic modulus in transferring heat and stress cannot be accurately simulated in uniaxial test pieces. Practical experience has shown that CGI can improve the service life of high performance direct injected diesel engine cylinder heads provided that the flame deck thickness is reduced to facilitate heat transfer and distribution of accumulated stress.

9 Damping Capacity

The damping capacity of cylinder block materials is frequently referred to in consideration of the anticipated NVH (Noise, Vibration and Harshness) performance of a finished engine. The ultimate noise level of an operating engine is dependent upon many factors including the stiffness of the cylinder block (derived both from the design of the block and the elastic modulus of the chosen material), interaction between excitation frequencies and local frequency modes, the influence of ancillary components such as pumps, belts and gears, and the damping capacity of the block material.

Damping capacity results are reported in the literature for several different types (chemistry, microstructure) of cast iron. The test and measurement techniques vary between references but are all based on the amount of reduction of the vibration wave amplitude during successive wavelength cycles. Results can be reported in terms of the Loss Factor (η), the logarithmic decrement (δ) or the damping capacity (ψ). Although these terms are interchangeable via the relationship : $\psi = 2\delta = 2\pi\eta$, it is most convenient to normalize results and present the relative damping capacity data on a scale of 0 to 1. Thus, the data from the literature are summarized in Table VIII.

Table VIII
Summary of relative damping capacity results from the literature

Reference Number	Gray Iron	CGI	Ductile Iron	Comment
32	1.0	0.53	0.37	All three irons were ferritic
33	1.0	0.35	0.14	"Similar" chemistry for all irons
34	1.0	0.38	0.19	Pearlitic CGI. Carbon equivalent = 4.0-4.3%
35	1.0	0.59	0.24	GG 25 vs. Ferritic CGI and SG
36	1.0	0.60	0.34	Microstructures not specified

In order to substantiate the literature results with more detailed microstructural data, a series of damping capacity tests were conducted at the Department of Vehicle Engineering of the Royal Institute of Technology (Kungliga Tekniska Högskolan) in Stockholm, Sweden. A total of 21 different as-cast microstructures were produced to represent various combinations of low (3.5-3.6%) and high (3.7-3.8%) carbon contents with low (70-80%) and high (95-100%) pearlite contents. Samples were cast over the entire range of graphite nodularity, including specimens with flake-patches. Conventional pearlitic grey iron (3.25% C) was included in the study as a reference material. All as-cast specimens were machined to provide test beams measuring (750x25x25 mm). The beams were suspended by two thin wires (free-free conditions) and excited near one end by a mechanical hammer. The vibrations were monitored by a 2 gram accelerometer attached near the

opposite end of the beam, but on the same face that was struck by the hammer. The data presented in this section represent the average values of five individual measurements at each resonant frequency. The measurements uncertainty was estimated to be 10%.

The damping capacity of a material is evaluated at its resonant frequency. Upon excitation, the 750 mm test beams developed seven different resonances ranging from 200 to 5000 Hz. In order to minimize the effect of microstructural variations in the long test beams, the relative damping capacity results (calculated from the logarithmic decrement) plotted in Figure 14 represent the average of the values measured at each of the seven resonant frequencies.

Figure 14 shows that the damping capacity decreases rapidly as the microstructure changes from Type A flake graphite to flake-patch and thereafter to CGI and higher nodularities. Relative damping capacities are on the order of Grey : CGI : SG = 1.0 : 0.35 : 0.22, although considerable scatter exists. For all practical CGI compositions, the damping capacity is independent of carbon content and pearlite content. Thus, it is concluded that damping capacity varies in relation to elastic modulus, as was also reported by Kurikuma et al [32]. Sergeant and Evans [34] and Subramanian et al [37] have reported that the damping capacity can be increased by 5-10% with increasing size or coarseness of graphite, however this factor could not be evaluated in the present study because the dimension and cooling rate of the as-cast test bars was kept constant for all specimens.
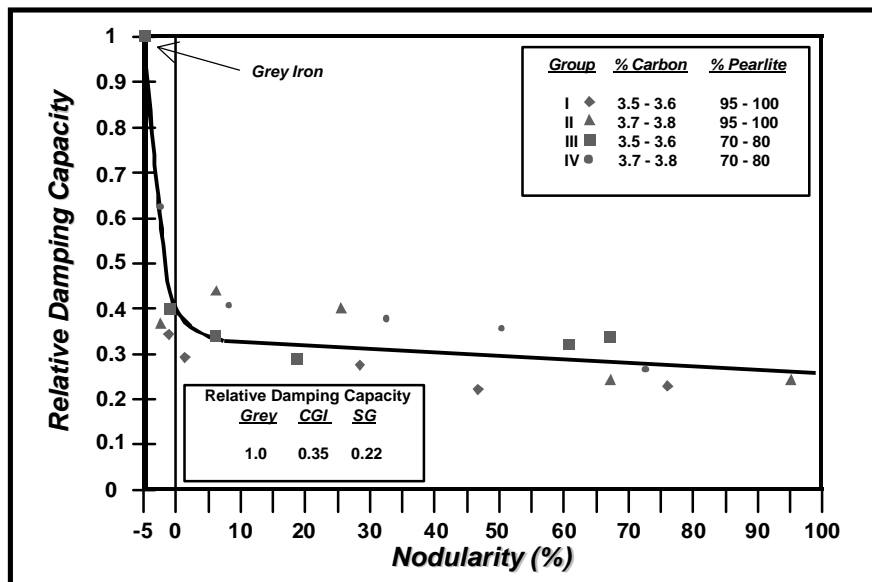

Figure 14: Relative damping capacity of cast irons as a function of nodularity, carbon and pearlite contents

While it is clear that CGI has a lower damping capacity than grey iron, this result must be taken in perspective. Relative damping capacity values for wrought aluminum alloys (normalized to grey cast iron) range from 0.004 [31] to 0.04 [38]. More specifically published values of the logarithmic decrement are on the order of 10^{-3} for cast iron and 10^{-5} or 10^{-6} for aluminum. However, the construction or boundary (design) effect even for a flat panel results in a logarithmic decrement on the order of 10^{-2} [39]. Thus, for commercially available cast irons and aluminum, the construction of the engine is significantly more important than the damping capacity of the material. Relative to identically designed grey iron blocks, modal analyses with fourteen different CGI cylinder blocks show an increase of 8-18% in the resonant frequency modes, which can be attributed to the 35% increase in elastic modulus of CGI relative to grey iron. This positive shift in vibration frequency has lead to 1.0 – 1.5 dB reductions in sound pressure levels of operating engines in semi-anechoic chamber tests [3].

10 Thermal Conductivity

The thermal conductivity of the graphite phase in cast irons is three to five times greater than that of either ferrite or pearlite [40]. It is therefore intuitively evident that the amount and shape of graphite are the critical factors in defining the thermal conductivity of cast irons. In order to quantify the effects of carbon content (in the practical CGI range of 3.5-3.8%), graphite shape, matrix composition and temperature on thermal conductivity, a series of controlled tests were conducted at the Austrian Foundry Institute (Österreichisches Giesserei-Institut, Leoben). The composition of the specimens, the test technique and the results are presented in this section.

The thermal conductivity specimens were cast as ASTM A 536 Y-block samples according to the method previously described for the tensile tests. Cylindrical samples (25 mm diameter by 25 mm long) were machined from the central area of the Y-block. Each specimen is 'stacked' in tight thermal contact between two reference materials of the same diameter and the thermal conductivity is evaluated by a comparative method with stationary axial heat flow. The upper reference specimen was coupled to a heat source while the lower reference was coupled to a heat sink. Radial heat losses were minimized by a guard heater and insulators. The reference material was SRM 8421 electrolytic iron supplied by the US National Institute of Standards and Technology.

Type N thermocouples were embedded at known locations in the cast-iron specimens and the reference materials. The temperature difference along the length of the specimen was approximately 10°C and the average value of the temperatures measured at the two thermocouple points was taken as the bulk temperature of the specimen. All measurements were conducted under argon atmosphere. The total uncertainty of the thermal conductivity results was estimated at 7%.

A total of 18 specimens were examined to determine the influence of carbon content, nodularity and pearlite content on thermal conductivity in the temperature range of 55-400°C. As shown in Table IX, the specimens were grouped into four broad categories of similar carbon (3.5-3.6%C and 3.7-3,8%C) and pearlite (70-80% and 95-100%) contents. The data, which are plotted in Figure 15 (a-d) thus show the change in thermal conductivity as a function of nodularity, pearlite content and temperature. Each line in Figure 15 is identified by its nodularity in parentheses which allows for cross-reference to the raw data contained in Table IX. The thermal conductivity of conventional pearlitic grey iron [4,38,41] is included in each of the Figure 15 plots as a reference.

The trends revealed in each of Figure 15 (a) through 15 (d) show that the thermal conductivity of CGI is approximately 25% less than that of pearlitic grey iron at room temperature and 15-20% less at 400°C. The observation that the thermal conductivity of grey iron decreases with increasing temperature is well known. However, it is interesting to note that even the presence of relatively small amounts of flake graphite in a predominantly compacted graphite microstructure also causes the conductivity to decrease with temperature. This is observed in the flake-patch specimens in each of the four microstructure groups. In contrast, the thermal conductivity of CGI and nodular cast irons gradually increases with increasing temperature. This is also in agreement with the literature which sometimes reports that the thermal conductivity of ferritic CGI can exceed that of pearlitic grey iron at temperatures above 200°C [16,42].

The trending of the thermal conductivity data presented in Figure 15 is logical, however the results show that compositional changes within the practical production range of 3.5-3.8% carbon can only influence the thermal conductivity by a maximum of 10%. While the microstructural latitude of CGI may be too narrow to significantly increase thermal conductivity, the data indicate that increases in nodularity from 10-30% cause a further 10% decrease in the thermal conductivity of CGI relative to grey iron. Therefore, it is more meaningful for CGI specifications to focus on avoiding high nodularity (and thus conductivity losses) in thermally loaded areas rather than trying to identify opportunities to increase conductivity. This is particularly true in consideration of the risk of the rapid decrease in tensile properties if flake graphite begins to appear in the CGI.
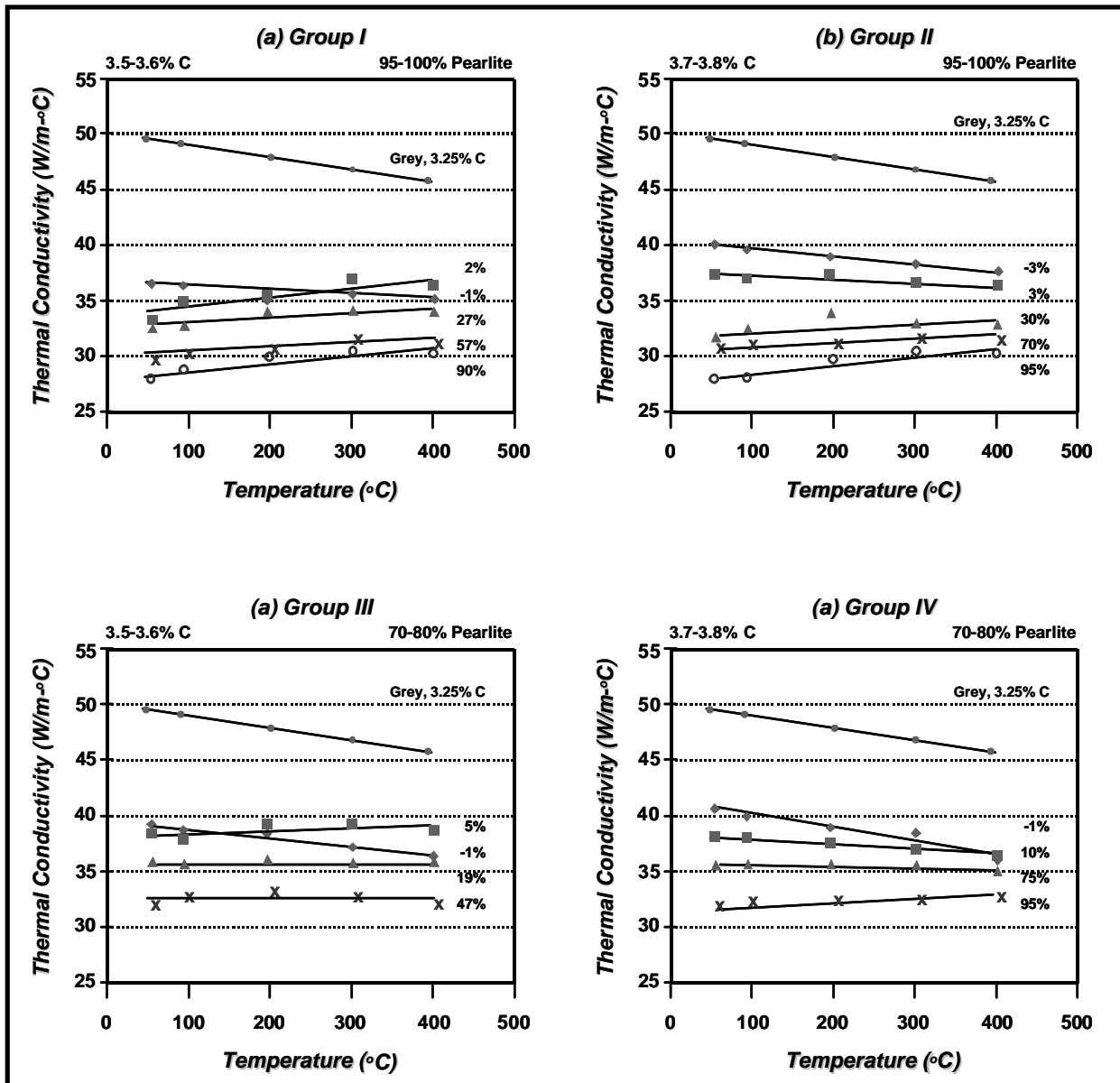

Figure 15: Thermal conductivity of cast irons as a function of nodularity, carbon content and pearlite content

SinterCast
— Supermetal CGI —

Microstructure Group	Sample Number	Nodularity (%)	Pearlite (%)	Chemical Analysis(%)								
				C	Si	Mn	S	Mg	Cu	Sn	Cr	Al
I	I-1	-1	95	3.49	2.13	0.43	0.014	0.006	0.77	0.07	0.03	0.008
(3.5-3.6%C)	I-2	2	95	3.48	2.12	0.43	0.015	0.008	0.77	0.07	0.03	0.008
(95-100%P)	I-3	27	98	3.49	2.18	0.43	0.012	0.015	0.77	0.07	0.03	0.007
	I-4	57	98	3.55	2.19	0.43	0.013	0.027	0.76	0.76	0.03	0.006
	I-5	90	100	3.60	2.22	0.45	0.015	0.032	0.75	0.75	0.04	0.007
II	II-1	-3	98	3.65	2.09	0.42	0.013	0.008	0.40	0.11	0.03	0.004
(3.7-3.8%C)	II-2	3	98	3.66	2.26	0.42	0.012	0.009	0.67	0.07	0.02	0.006
(95-100%P)	II-3	30	100	3.74	2.35	0.42	0.013	0.020	0.66	0.08	0.02	0.005
	II-4	70	98	3.82	2.41	0.41	0.011	0.013	0.83	0.09	0.03	0.009
	II-5	95	98	3.81	2.42	0.40	0.009	0.022	0.84	0.09	0.03	0.009
III	III-1	-1	80	3.50	2.12	0.41	0.015	0.009	0.55	0.04	0.03	0.008
(3.5-3.6%C)	III-2	5	80	3.57	2.10	0.40	0.012	0.011	0.52	0.04	0.02	0.008
(70-80%P)	III-3	19	80	3.58	2.15	0.40	0.014	0.015	0.51	0.04	0.03	0.008
	III-4	47	70	3.57	2.10	0.38	0.010	0.022	0.51	0.04	0.03	0.003
IV	IV-1	-1	70	3.66	2.09	0.41	0.012	0.007	0.39	0.05	0.03	0.005
(3.7-3.8%C)	IV -2	10	70	3.73	2.35	0.39	0.013	0.009	0.55	0.04	0.03	0.007
(70-80%P)	IV -3	75	70	3.75	2.36	0.39	0.013	0.013	0.55	0.04	0.03	0.005
	IV -4	95	80	3.69	2.42	0.41	0.010	0.020	0.48	0.07	0.03	0.005

11 Summary

The graphite shape, carbon content and pearlite content of cast irons each play an important role in determining the mechanical and physical properties of cast irons. While some material properties, such as Poisson's ratio or thermal expansion, are effectively constant over a wide range of microstructure and chemistry, the present study addresses the effect of microstructural changes on the properties of compacted graphite iron.

The mechanical properties of CGI decrease by 20-25% as soon as flake-type graphite appears in the microstructure. Although the mechanical properties gradually increase as the nodularity exceeds 20%, thermal conductivity is reduced and castability and machinability become more difficult. The data obtained at increased nodularity levels also serve to indicate the expected change in material properties as the nodularity varies between thin and thick sections of a casting, which can be used to advantage in CGI engine design. Although the demands of every component are unique, the data suggest that a nodularity range of 0-20% is appropriate for the cylinder bore walls and other structural regions of a cylinder block. Flake graphite is inadmissible. The pearlite content, which is linearly related to hardness and tensile strength, can be specified to suit the wear, machinability and high temperature performance requirements of the component. Alloying elements can also be specified to improve selected properties.

12 References

1 Sonderheft 10 Jahre TDI: MTZ Motortechnische Zeitschrift, Okt, 1999. To be published.

2 D-Moment, Auto Motor und Sport, Issue 10 1999, pp. 92-94.

3 F. Indra, M. Tholl, "Compacted graphite iron (CGI) - A new material for internal combustion engines", Fifth Aachen Colloquium on Vehicles and Automobile Technology, pp 331-350 (1995).

4 I.C.H. Hughes and J. Powell, 'Compacted Graphite Irons - High quality engineering materials in the cast iron family', SAE Paper 840772, 1984.

5 J.D. Altstetter and R.M. Nowicki, 'Compacted Graphite Iron - Its properties and automotive applications', AFS Transactions 82-188, 1982, pp. 959-970.

6 C.R. Loper, M.J. Lalich, H.K. Park and A.M. Gyarmaty, 'The relationship of microstructure to mechanical properties in compacted graphite irons', AFS Transactions 80-160, 1980, pp. 313-330.

7 E. Nechtelberger, The properties of cast iron up to 500°C, English edition published in 1980 by Technicopy Ltd, England; German edition published in 1977 by Fachverlag Schiele und Schön GmbH, Germany.

8 K. Röhig, 'Gusseisen mit vermiculargraphit-herstellung, eigenschaften, anwendug', Konstruieren + Giessen, Vol. 16, No. 1, 1991, pp. 7-27.

9 D.M. Stefanescu, R. Hummer and E. Nechtelberger, 'Compacted Graphite Irons', Metals Handbook, Ninth Edition, Vol. 15, 1988, pp. 667-677.

10 T. Okamoto, A. Kagawa, K. Kamei and H. Matsumoto, 'Effect of graphite shape on thermal conductivity, electrical resistivity, damping capacity and Young's modulus of cast iron below 500°C', Journal of Japan Foundrymen's Society, Vol. 55, No. 2, 1983.

11 Y. Tanaka, H. Saito, K. Ikawa, 'Relation between graphite structure and physical and mechanical properties of compacted/vermicular graphite cast iron', Journal of Japan Foundrymen's Society, Vol. 53, No. 4, 1981.

12 SinterCast Nodularity Rating Charts, SinterCast, 1997.

13 Y. Gu, Ford Motor Company Ltd, "Engine cylinder block", European Patent Application EP 0 769 615 A1, (April 23, 1997).

14 Mazda Motor Corporation, "Ductile iron cylinder block with grey iron bore region", Japanese Patent 6-106331, (April 19, 1994).

15 G.F. Ruff, 'Mechanical properties of compacted graphite cast iron', SAE Paper 810209, 1981.

16 E. Nechtelberger, H. Puhr, J.B. van Nesselrode and A. Nakayasu, 'Cast iron with vermicular/compacted graphite - state of the art', International Foundry Congress, Chicago, April 1982, pp. 1-39.

17 J.P. Hrusovsky, Formation, production and properties of compacted graphite iron, Ph.D. Thesis, Case Western Reserve University, Cleveland, Ohio, 1982.

18 F.K. Bobylev, A. S. Glinkin, N.N. Aleksandrov and V.I. Popov, 'Compacted graphite iron for D50 cylinder liners', Russian Castings Production, November 1976, pp. 445-446.

19 Riposan, M. Chisamera and L. Sofroni, 'Contribution to the study of some technological and applicational properties of compacted graphite cast iron, AFS Transactions, 85-07, 1985, pp. 35-48.

20 S. Hogmark, J. Alander, 'Wear of cylinder liners and piston rings', Wear of Materials, Virginia, pp 38-44 (1983)

21 L. Lundin, Volvo Technological Development AB Technical Report, "Wear properties of compacted graphite iron (CGI): a comparison with Volvo truck company's standard grey iron D10 liners", 27 March 1988.

22 K. B. Palmer, 'Mechanical properties of compacted graphite iron', BCIRA Report 1213, 1976, pp. 31-37.

23 M. Shikida, Y. Kanayama and H. Nakayama, 'Strength and crack growth behaviours of compacted graphite vermicular cast iron in rotating bending' (in English), 29th Japan Congress on Materials Research, 1986, pp. 23-28.

24 T. Maezono, Y. Ohtsuka, R. Takahashi and K. Otsuka, 'Fatigue crack growth of spheroidal graphite and compacted/vermicular graphite cast iron' (in Japanese), Journal of Japan Foundrymen's Society, Vol. 56, No. 11, 1984, pg 658.

25 T. Shiota and S. Komatsu, 'Influence of notch effect and effective sectional area on fatigue strength of cast irons with various graphite shape' (in Japanese), Journal of the Society of Materials Science of Japan, Vol. 27, No. 294, 1978, pg 291.

26 H. Suzuki, M. Ouyabu, T. Ueki and T. Kunio, 'Influences of microstructure and mechanical properties on fatigue strength of compacted vermicular and nodular cast iron' (in Japanese), Journal of the Society of Material Science of Japan, Vol. 50, No. 451, 1984, pp. 520-525.

27 M. Shikida, Y. Kanayama and H. Nakayama, 'Fatigue strength, crack growth rate and fracture appearance in compacted graphite vermicular graphite cast iron' (in Japanese), Journal of Material Science Japan, Vol. 36, No. 404, 1987, pg. 455.

28 H. Sumimoto, K. Nakamura and Y. Umeda, 'Relationship between graphite morphology and fatigue limit in compacted vermicular and ductile cast iron' (in Japanese), Kinki University Research Report, Vol. 22.

29 K.R. Ziegler and J.F. Wallace, 'The effect of matrix structure and alloying on the properties of compacted graphite iron', AFS Transactions, 84-123, pp. 735-748.

30 Y.J. Park, R. B. Gundlach and J.F. Janowack, 'Effects of molybdenum on thermal fatigue resistance of ductile and compacted graphite irons', AFS Transactions, 87-90, pp. 267-272.

31 Iron Castings Handbook, C.F. Walton and T.J. Opar (Eds), Iron Castings Society, Cleveland, Ohio, 1981.

32 T. Kurikuma, Y. Makimura, M. Tada and T. Kobayashi, 'Effects of graphite morphology and matrix microstructure on damping capacity, tensile strength and Young's modulus of casting irons' (in Japanese), J. of Japan Engineering Society, Vol. 68, October 1998, pp 876-882.

33 A. A. Usol'tev, 'Damping capacity of vermicular graphite cast iron', Steel in the USSR, Vol. 20, October 1990, pp. 503-504.

34 G. F. Sergeant and E.R. Evans, 'Production and properties of compacted graphite irons', BCIRA Publication 1978.

35 A. Visnapuu, B. A. Betts and L. A. Neumeier, 'Influence of graphite morphology on the damping properties of selected cast iron structures', Rolla Research Centre, Bureau of Mines, U.S. Dept of Interior, Rolla, Mo. 65401, USA, 1977.

36 R. D. Schelleng, 'Cast iron with at least 50% of the graphite in vermicular form and process for making same', United States Patent 3,421,886, 14 January 1969.

37 S. V. Subramanian and A. J. Genualdi, 'Optimization of damping capacity and strength in hyper-eutectic grey cast iron, AFS Paper 96-138, American Foundrymen's Society, 1996, pp. 1-2

38 Smithells Metals Reference Book, Seventh Edition, E. A. Brandes and G. B. Brook (Eds), Butterworth, 1992.

39 Noise and Vibration Control, Revised Edition, L.L. Beranek (Ed.), Inst. of Noise Control Engineering 1988, pg. 449.

40 H.T. Angus, Cast Irons: Physical and engineering properties, Second Edition Butterworths, 1976.

41 D.B. Craig, M.J. Hornung and T.K. McCluhan, 'Grey Iron', ASM Handbook, Vol. 15, ASM 1988, pg. 644.

42 P.A. Blackmore and K. Morton, 'Structure-property relationships in graphite cast irons', Int. J. Fatigue, July 1982, pp 149-155.

For further information please see our website
www.sintercast.com